Full Text View

Thermohaline Circulation Studies with an Isopycnic Coordinate Ocean Model

Shan Sun

NASA Goddard Institute for Space Studies, New York City, New York

Shan Sun and Rainer Bleck

Los Alamos National Laboratory, Los Alamos, New Mexico

ABSTRACT

The thermohaline circulation (THC) in a 1000-yr near-global numerical simulation using the Miami Isopycnic Coordinate Ocean Model is analyzed and compared to observations. The model, driven by observed monthly atmospheric climatology, uses potential density referenced to 2000 m (σ_2) as the vertical coordinate and accounts for compressibility (thermobaricity) effects. Examination of the three-dimensional mass flux field reveals that the model comes fairly close to quantitatively reproducing a number of global and basin-scale circulation features, such as the vertical–meridional overturning rate in the three major basins, the meridional heat flux, and the transport through the major passages. Methods are presented that allow the construction of composite diagrams revealing quantitative *regional* aspects of the modeled circulation in potential density space. The diagrams reveal many features of the modeled THC that adhere to observations, the most noticeable shortcoming being a weaker-than-observed northward penetration of bottom water into the three major basins caused by insufficient production of Antarctic Bottom Water.

1. Introduction

After decades of effort aimed at a comprehensive description of the global ocean circulation, a coherent picture is beginning to emerge. Stommel (1957, 1964, 1965) applied the basic hydro- and thermodynamic equations to an idealized ocean and constructed a circulation diagram depicting sinking at high latitudes, upwelling both at low latitudes and in the Antarctic Circumpolar Current (ACC), and associated horizontal motion systems controlled by various physical processes. Gordon (1986), in search of the water source feeding the North Atlantic Deep Water (NADW) production mechanism, presented a

two-layer picture of the global circulation where NADW moves southward across the equator in the lower layer and joins the ACC while some of it upwells into the upper layer in the interior of the subtropical gyres in the Atlantic Ocean and in the ACC. This is fairly consistent with the picture developed by Stommel. The new element in Gordon's scheme is that the deep (cold) water that enters the Pacific and Indian Oceans from the ACC, upwells there into upper (warm) layers in the interior of the subtropical gyres, subsequently flows through the Indonesian passage(s), joins the Agulhas Current, and rounds the Cape of Good Hope, eventually finding its way into the North Atlantic where it completes the upper branch of the circulation.

Broecker (1991) elaborated on this picture by sketching a closed loop of the global thermohaline-forced circulation (THC), which he named the "global conveyor." Rintoul (1991) proposed that the upper-layer compensatory flow for the formation of NADW enters the South Atlantic through Drake Passage, mostly as upper intermediate water[1] (the cold water path), in contrast to the suggestion by Gordon (1986) that this compensatory flow enters the South Atlantic from the Indian Ocean as upper-layer water (the warm water path). Schmitz (1995, 1996a,b) found that both paths are important and possibly of equal significance (transport), but that at least three layers are required to depict this configuration, with four layers needed in order to also describe bottom water–deep water interactions. Schmitz (1995, 1996a,b) also identified possible sites for upwelling that are layer and path specific, located, for example, in the northern Indian Ocean and the South Pacific Ocean and in equatorial zones as well as in the ACC.

Various methods have been used in the past to describe the THC, including trajectory methods in regional level models (Döös 1995) and inverse methods from hydrographic data (Macdonald and Wunsch 1996). In this study we take advantage of the ability of isopycnal models to classify and track water masses as we set out to examine the relation of key features of the modeled global THC to observation-based summaries. The model used for this purpose is a near-global version of the Miami Isopycnic Coordinate Ocean Model (MICOM) configured with a low horizontal resolution (1.4°) and 16 layers (Bleck et al. 1992, 1997; Sun 1997; Sun et al. 1999).

Isopycnic coordinate models naturally decompose the three-dimensional oceanic circulation into its isopycnal and diapycnal components, allowing one to sketch the circulation simulated by the model in much the same way as was done in the observational studies referenced above. Perhaps more importantly, the numerical properties that make this decomposition easy also prevent numerical truncation errors in the model from acting as sources of diapycnal mixing. Indeed, by comparing numerical simulations in depth and isopycnic coordinates, Roberts et al. (1996) and Chassignet et al. (1996) have demonstrated that isopycnic coordinate models retain abyssal water properties more faithfully than depth coordinate models. These authors have also pointed out that the presence of a diapycnal component in the *lateral* mixing scheme has a strong impact on the meridional overturning circulation and the associated heat flux, and on the evolution of water masses. Isopycnic coordinate ocean models, which carry out lateral mixing along approximately neutral coordinate surfaces, have a natural advantage in describing these global transport processes.

Only a few classes of model errors can be eliminated by manipulating the vertical coordinate. Other errors having to do with insufficient horizontal resolution, simplification of model physics, and uncertainties in the atmospheric forcing functions, remain. These errors inevitably lead to differences between the model-rendered circulation and observational summaries, which are themselves approximations. In documenting these differences, the authors hope to provide guidance to future work, both observational and modeling. The work presented here, an extension of the work by Sun (1997), employs model–data intercomparison techniques briefly described in Sun (1997) and Bleck (1998). A more detailed description of these techniques will be given here.

2. Model setup

The use of potential density as vertical coordinate in ocean circulation models leads to a particularly simple formulation of model dynamics if temperature-dependent compressibility variations (thermobaricity) are ignored. However, thermobaricity is known to lead to folding and nonneutrality of σ_0 surfaces in the deep ocean ($\sigma_0 = \rho_0 - 1000$ kg m^{-3}, where ρ_0 is potential density referenced to sea level). Sun et al. (1999) have devised a method for including thermobaricity in the isopycnic model physics and have proposed to reduce folding and nonneutrality of coordinate surfaces by using σ_2, potential density referenced to 20 MPa (roughly 2000 m), as the vertical coordinate. The MICOM version used here includes these two innovations.

The model domain used in this study covers the region from 66°N to 69°S, the domain size typically chosen for "global" models lacking a sea ice component. A regular grid on a Mercator projection is used with a resolution of 1.4° × 1.4° cos (lat). There are 16 layers in the vertical, including a surface mixed layer with horizontally and temporally variable density and 15 isopycnic layers beneath. The 15 coordinate values, in σ_2 units, are 33.22, 34.26, 35.04, 35.62, 36.05, 36.37, 36.61, 36.79, 36.92, 37.01, 37.07, 37.11, 37.14, 37.17, and 37.20 kg m^{-3}. The bottom topography is obtained by spatially integrating ETOPO5 data of 5′ spatial resolution over each grid cell. No further smoothing is done, but the minimum water depth is set to 150 m to avoid instabilities associated with wave breaking in the model's "surf zone."

No effort has been made to bring the various sill depths in the model into agreement with observed depths, nor is turbulent mixing in dense overflows incorporated into the model physics at present. Work on the latter is in progress.

Following Sun et al. (1999), the potential density of seawater in individual model layers is expressed by its "virtual potential density"

$$\rho^*_{\text{pot}} = \rho_{\text{pot}}(1 + \kappa^{(\theta)}(p - p_{\text{ref}})), \quad (1)$$

where p_{ref} is 20 MPa and $\kappa^{(\theta)}$ is the thermobaric component of compressibility. There are some trade-offs in defining the local pressure p in layer model applications of (1). With ρ_{pot} being a "layer" variable (i.e., a variable treated as vertically constant within a coordinate layer), it would seem natural to evaluate (1) using a p value representing the pressure at middepth in each layer. However, this allows the bottom interface pressure to affect p, which in turn can lead to nonphysical ρ^*_{pot} variations—and hence pressure forces—in layers whose lower interface coincides with a potentially bumpy seafloor. For this reason, p in (1) is defined in the present MICOM implementation as the pressure on the *upper* interface of each layer. One exception to this rule is in the mixed layer entrainment/detrainment algorithm where, for the purpose of evaluating the buoyancy contrast between the mixed layer and the layer beneath, ρ^*_{pot} in the mixed layer is evaluated using p at the mixed layer *bottom*.

In the experiments reported here, all surface forcing fields were computed from time-interpolated monthly climatological atmospheric fields. The prescribed atmospheric fields include

- temperature and relative humidity from the Comprehensive Oceanographic and Atmospheric Data Set (COADS; Woodruff et al. 1987),

- surface wind stress and friction velocity from COADS, blended south of 50°S with stress fields from the European Centre for Medium-Range Weather Forecasts,

- net radiation flux from the Oberhuber (1988) atlas, and

- precipitation from the NOAA microwave sounder (Spencer 1993).

Latent and sensible heat fluxes were computed using conventional bulk formulas. We added a total of 0.65 Sv (Sv $\equiv 10^6$ m^3 s^{-1}) of river runoff at 14 outflow points, supplemented by 0.18 Sv of Arctic and 0.27 Sv of Antarctic meltwater runoff (Brown et al. 1989, their Fig. 6.33) evenly distributed along the northern and southern domain boundary, respectively. River runoff is treated as a smeared-out point source added to the precipitation field at coastal outflow locations.

Smoothing of isopycnal layer interfaces, which in isopycnic models is commonly done to suppress small-scale noise, gives rise to "bolus fluxes," which for all intents and purposes are identical to those introduced by Gent and McWilliams (1990) into Cartesian coordinate models. Since isopycnals are typically bowl-shaped in the vertical–meridional plane (most outcrop in both hemispheres), Laplacian smoothing would have a systematic shoaling effect on layer interfaces. MICOM therefore uses a biharmonic formulation for interface smoothing.

An important parameter in long-term simulations is the diapycnal diffusivity coefficient K_v. In this run we use a value inversely proportional to the buoyancy frequency N, $K_v = 0.002$ (cm^2 s^{-2})/N. Interior diapycnal mixing is modeled in MICOM using a scheme developed by McDougall and Dewar (1998).

The model simulation was started from a motionless state and a 16-layer structure based on annual temperature and salinity data from the Levitus and Boyer (1994) and Levitus et al. (1994) climatology. The near-global version of MICOM has northern and southern boundaries that act as solid walls. This geometry excludes the Greenland–Norwegian Sea and the southern fringe of the Southern Ocean, which are the main sources of NADW and Antarctic Bottom Water (AABW), respectively. In an attempt to compensate for the absence of these basins, downward diapycnal fluxes of specified strength are imposed next to the northern and southern boundaries. These lateral boundary conditions transfer 3 Sv from lighter layers into model layer 16 in the boundary region adjacent to the Weddell Sea and a total of 6 Sv from lighter layers into model layer 14 in two regions east and west of Iceland. For observational evidence concerning the magnitude of these fluxes the reader is referred to Mauritzen (1993, 1996a,b), Speer and Zenk (1993), Price and Behringer (1994), Schmitz (1995, 1996a,b), and Orsi et al. (1999).

3. Model results

a. Layer mass census

An analysis of the kind presented below ideally should be based on model fields that are in near-steady state and, at the same time, are close to observed conditions. Due to a variety of reasons, among them uncertainties in the atmospheric forcing and the diapycnal mixing parameterization (especially in the surface mixed layer and in sill overflows), this goal remains elusive today.

In isopycnic models, the total mass in each of the model layers is a convenient measure of model drift. To demonstrate the extent of model drift, we show in Fig. 1 ⊙ the temporal evolution of horizontally averaged layer thickness for each of the 16 model layers, as well as the drift of globally averaged temperature and salinity, for the experiment mentioned. The curves are based on four data points per year. The apparent variations in curve thickness provide some measure of seasonal variability of globally averaged layer thickness.

In Fig. 1 ⊙, several middepth layers are seen to expand by hundreds of meters during the first few centuries at the expense of layers above and below. These trends suggest deficiencies in modeling the subduction process—deficiencies that in turn stem from the aforementioned inaccuracies in atmospheric forcing and/or oversimplification of mixed layer physics. (MICOM uses a Kraus–Turner slab mixed layer.)

The bottom two curves in Fig. 1 ⊙ reveal a global temperature and salinity increase of nearly 0.62°C and 0.12 g kg^{-1} in the course of the 1000-yr run. The model's inability to conserve salt is a result of our prescribing freshwater input (alias salt loss) from precipitation and river/glacier runoff in the form of a model state-independent surface flux, while allowing evaporative freshwater loss (alias salt gain) to be calculated on the basis of the modeled SST and a prescribed atmospheric humidity field. Efforts to reach a balance between freshwater gain and loss in our simulations have been largely unsuccessful, mainly because adding freshwater typically stabilizes the water column (i.e., reduces the mixed layer depth), which in turn raises the SST and enhances evaporation.

To illustrate the effect of the layer thickness changes shown in Fig. 1 ⊙ on the stratification in individual basins, representative meridional cross sections are shown in Fig. 2 ⊙ to highlight the migration of isopycnal layer interfaces during the 1000-yr run (a) in the Atlantic and (b) in the Pacific. The N-dependent diffusivity coefficient used here enhances abyssal diapycnal mixing, according to Fig. 2 ⊙, in a way that results in a slight warming of portions of the deep ocean. The thickness decrease indicated in Fig. 1 ⊙ for the upper 5 isopycnic layers indicates a gradual loss of light- and medium-density water in the model, leading to a pronounced shoaling of the thermocline.

Figure 3 ⊙ presents the interface drift during the 100-yr interval chosen for our present analysis. The most noteworthy feature in Fig. 3 ⊙ is the continuing buildup of the deep and bottom water in the Atlantic, while conditions in the Pacific at this time are more nearly stationary.

b. Diapycnal diffusivity

The Bjerknes circulation theorem (specifically, the solenoidal term $\oint dp/\rho$) tells us that surface density contrasts must be distributed over a finite pressure interval before they can drive circulations. Diapycnal mixing therefore is an important part of maintaining the THC. A number of millennial runs were carried out with different diapycnal diffusivity coefficients [K_v = 0, 0.001, · · ·, 0.003 (cm^2 s^{-2})/N, 0.1, · · ·, 0.3 cm^2 s^{-1}] to investigate the sensitivity of the modeled circulation to the formulation of K_v.

As expected, we found the THC to be stronger for larger K_v values. Furthermore, as K_v reached zero, we saw a tendency in the zonally averaged overturning circulation away from a meridionally symmetric pattern (upwelling near the equator) to a single interhemispheric cell (upwelling in the Southern Ocean).

The diffusivity values in the model run chosen for further analysis, 0.002 (cm^2 s^{-2})/N, represent a compromise between the needs to (i) minimize unbalanced production of dense water, that is, model drift and (ii) reduce the background diffusivity to "typical" open ocean values of order 0.1 cm^2 s^{-1} (Toole et al. 1994a). Since MICOM at its present stage of development has no provisions for regionally enhanced vertical mixing, the chosen compromise values inevitably overemphasize open ocean mixing and thus assign the Pacific, due to its sheer size, a somewhat larger role in cold-to-warm water mass conversion than it has in reality.

The diagnostic methods presented below were applied to several 100-yr periods, specifically, years 500–600 and years 900–1000. The resulting circulation figures were found to have many features in common. Due to space limitations, we will only present results from one 100-yr period, years 900–1000.

While the ocean state has drifted away from the initial conditions by year 1000, the chosen period represents a time window characterized by relatively small transients in the hydrographic makeup of the model ocean.

c. Vertical–meridional overturning

Streamfunctions expressing the strength of the meridional overturning circulation in individual model basins can be obtained by zonally integrating the meridional isopycnal mass flux component in each basin layer by layer and then vertically summing up the values so obtained. Figure 4 shows the time evolution of the maximum streamfunction value (or overturning rate) in the Atlantic from this experiment. The overturning rate stabilizes around 22.7 Sv, at the high end of the estimate of 18 ± 4 Sv (Macdonald 1998). Note, however, that instantaneous overturning rate maxima are typically higher than maxima obtained from time-averaged flux fields because the location of the streamfunction peak in the vertical–meridional plane tends to move back and forth with time.

Time-averaged overturning streamfunctions in each of the major ocean basins and the World Ocean as a whole, averaged over years 900–1000, are displayed in Fig. 5 in latitude–density space. The discontinuity one would expect in the Indian and Pacific basin streamfunction plots due to water entering/exiting through the Indonesian passage has been eliminated in these figures by adding a clockwise circulation around Australia equal in strength and water mass composition, but opposite to, the Indonesian Throughflow.

Note that streamfunctions based entirely on the isopycnal mass flux, such as the ones shown here, capture the *total* vertical displacement of water particles, rather than the component associated with diapycnal mixing; these two measures of the vertical mass flux agree only under steady-state conditions. Judging from the interface migration rates indicated in Fig. 3, the true diapycnal fluxes in this simulation differ from the ones shown in Fig. 5 by no more than a few tenths of Sverdrups.

As seen in Fig. 5a, the meridional circulation in the Atlantic basin is dominated by an interhemispheric overturning cell composed of water entering the basin as low-density water from the south and returning as high-density water. The circulation in the Pacific (Fig. 5b) is characterized by a pair of shallow, wind-driven circulation cells centered on the equator and by an abyssal cell composed of water entering the basin as high-density water from the south and exiting as a mixture of intermediate and surface water. The Indian Ocean streamfunction plot (Fig. 5c) reveals weak upwelling largely confined to the Southern Hemisphere. Note that a counterclockwise rotation around Australia equal in strength to the Indonesian Throughflow should be added to flow estimates based on Figs. 5b and 5c before quantitatively comparing the strength of the Indian and Pacific basin overturning cells to observations. A portion of the upper and intermediate water pictured in Fig. 5b as flowing southward within the confines of the Pacific basin actually exits through the Indonesian passage and flows south in the Indian Ocean.

The circulation in the World Ocean (Fig. 5d), obtained by adding the streamfunction patterns from Figs. 5a–c and adding the Southern Ocean, is dominated by the interhemispheric Atlantic cell. The overall circulation pattern conforms to generally held notions (e.g., Fig. 6.15 in Brown et al. 1989) in that it shows a wedge of NADW flanked above and below by lobes of a thermally direct southern cell representing, respectively, AABW and AAIW production.

The model-generated zonally averaged meridional heat flux in the global ocean and in each individual basin as a function of latitude during the same period is shown in Fig. 6a. For comparison, the heat flux estimate derived by Trenberth and Solomon (1994, hereafter TS) from the observed surface flux is plotted in Fig. 6b on the same scale.

MICOM experiments in the truncated near-global domain described earlier typically produce a maximum Atlantic heat flux of around 0.8–0.9 PW, close to what TS show in Fig. 6b. The model-generated heat fluxes in the North and South Pacific are around 0.75 PW and −0.95 PW, respectively, which are weaker than what TS obtained. The modeled maximum heat flux in the southern Indian Ocean is −0.24 PW, much weaker than the -0.93 ± 0.19 PW obtained by TS, but close to the -0.42 ± 0.19 PW from Robbins and Toole (1997).

Heat flux estimates in situations characterized by a nonzero net mass flux, as is the case in both the Indian and the Pacific basins due to the presence of the Indonesian passage, are ambiguous. (For example, nonzero net mass flux creates "phantom" heat fluxes even in an isothermal ocean; their magnitude depends on where the analyst places the zero point on the temperature scale.) We deal with this ambiguity by disregarding the heat transported by the counterclockwise circulation around Australia whose strength is set by the Indonesian Throughflow. Specifically, we compute the heat flux through the Indonesian passage and add/subtract this value to/from the northward heat flux in the Indian/Pacific Ocean at all latitudes south of the throughflow point. The discrepancies between our heat flux estimates and those of TS and Robbins and Toole

(1997) are in part due to different conventions employed in dealing with this ambiguity.

d. Drift at the surface and Drake Passage Throughflow

The SST differences between years 1 and 1000, shown in Fig. 7a ⊙▬, are dominated by the side effects of a gradual loss of western boundary current inertia typical for coarse-resolution simulations, namely, cooling (by several °C) on the warm side and warming on the cold side of the boundary currents. The equatorial cold tongue in the eastern Pacific is too cold by several degrees Celsius. The surface salinity fields in Fig. 7b ⊙▬ indicate increased salinity, by a few tenths of a gram per kilogram in the Indian and Southern Ocean, and freshening in the Pacific between 40°S and 40°N.

Figure 8 ⊙▬ shows the annually averaged Drake Passage throughflow obtained in the experiment over the 1000-yr period. The throughflow starts with 129 Sv in the first decade, in the observed range of 123 ± 10.5 Sv (Whitworth and Peterson 1985). It gradually declines and stabilizes around 108 Sv in the last century.

e. Tracer advection experiments

Tracers are a time-honored tool for investigating circulation and mixing patterns and for tracking the spreading of major water masses in the ocean. In order to get a closer look at the pathways of NADW in the model, we have added a passive tracer to isopycnal layers outcropping in the Labrador Sea. (Our method of locating isopycnal layer outcrops in the archived data—essentially a scheme that apportions MICOM's slab mixed layer among the various isopycnal layers—will be discussed in the next section.) Mass fluxes averaged over model years 500–600 are used in perpetual mode to advect the tracer isopycnally and diapycnally throughout the World Ocean. The injection algorithm maintains 100% tracer concentration between the surface and the first layer interface deeper than 10 m. Most of this material is then advected and mixed isopycnally within the "seeded" layers, while diapycnal mixing causes some material to seep across interfaces into other layers.

We will show here the tracer distribution at $\sigma_2 = 37.01$, the layer closest to $\sigma_2 = 37.00$ where the NADW salinity maximum core south of Africa is found by Mantyla and Reid (1995). The progress of the seeded water masses is displayed in terms of tracer amount, that is, by the product of concentration and layer thickness. Hence, the values represent the equivalent depth of a layer of water saturated with tracer. Figure 9 ⊙▬ depicts the tracer amount so defined 25, 50, 100, and 200 years after commencement of tracer injection. A logarithmic scale is used for the gray shade intensity to capture small tracer amounts.

In the pattern sequence, the tracer added to layer $\sigma_2 = 37.01$ at its outcropping location is carried by the NADW southward along the American continent. Tracer plots not shown here indicate that the material reaches the equator in about 15 years. By year 25, the tracer-laden tongue has reached a thickness of 200 m at the equator. A (slightly split) tracer tongue is seen to extend eastward along the equator. Speed, route, and shape of the equatorial jet of NADW are in qualitative agreement with CFC observations of Smethie et al. (1999). In the high-latitude North Atlantic, tracer is seen to invade the eastern subbasin through the Charlie–Gibbs Fracture Zone.

By year 50 (Fig. 9b ⊙▬), the Labrador Sea tracer has reached the southern Atlantic, and some of it has already been carried by the ACC well past Cape of Good Hope into the Indian Ocean. By year 100, some tracer material moving with the ACC has completed the circumnavigation of the Southern Ocean, that is, has reentered the Atlantic through Drake Passage (Fig. 9c ⊙▬). At the same time, tracer is seen moving northward along the Tonga Escarpment and is about to reach the equator in the eastern Pacific.

Two paths from the Southern Ocean into the Indian Ocean can be distinguished in Fig. 9c ⊙▬: a weak eastern path between the Ninety East Ridge and Australia, and a more prominent one between Madagascar and the Central Indian Ridge, in agreement with observations by Mantyla and Reid (1995).

Meanwhile, in the Atlantic Ocean, the tracer has crossed the Atlantic Ridge, mostly through the Vema and Romanche Fracture Zones, and has occupied most of the eastern basin (Figs. 9b and 9c ⊙▬).

By year 200 (Fig. 9d ⊙▬), tracer-laden water is seen to occupy large portions of the North Pacific.

In the Indian Ocean, water advancing along both sides of the Ninety East Ridge has reached the equator, while a substantial amount of tracer following the western path has entered the northern Indian Ocean.

Figure 9 ⊙▬ conveys an idea of the time required for water masses originating in the northern North Atlantic to spread in the World Ocean, and what approximate paths they take. Analogous tracer spreading plots focusing on abyssal water masses originating in the Weddell Sea have been constructed but will not be shown here for lack of space.

f. A mass flux aggregation scheme

The tracer distribution shown in Fig. 9 indicates rates and pathways for NADW spreading but only provides a vague estimate of mass transport. In order to extract quantitative information from model output for comparison with observational estimates, the 15 isopycnal model layers are lumped into four density classes, referred to hereafter as

- *upper* water ($\sigma_2 \leq 36.05$) including Subtropical Mode Water: layers 1–5;

- *intermediate* water ($36.37 \leq \sigma_2 \leq 36.79$) including Antarctic Intermediate Water (AAIW), Subpolar Mode Water (SPMW), Subantarctic Mode Water (SAMW): layers 6–8.

- *deep* water ($36.92 \leq \sigma_2 \leq 37.11$) including Upper NADW (UNADW), Middle NADW (MNADW), Circumpolar Deep Water (CDW), and Labrador Sea Water (LSW): layers 9–12;

- *bottom* water ($\sigma_2 \geq 37.14$) including Lower NADW (LNADW) and AABW: layers 13–15.

For obvious practical reasons, the division of the ocean into different classes had to be done in terms of model coordinate layers and so does not completely match the class structure of Schmitz (1995). Likewise, the correspondence between classes and water masses has to be taken with a grain of salt. The averaged mass flux is then calculated within each class and across the three class interfaces for the 100-yr period following model year 900.

Since the mixed layer in MICOM is a nonisopycnic coordinate layer and thus does not naturally fall into one of the four chosen density classes, mixed layer mass fluxes are assigned for analysis purposes to whichever isopycnic layer most closely matches the mixed layer density at a particular instant and location. This manipulation in effect extends all isopycnic coordinate layers, which for numerical reasons are treated in the model as terminating at the mixed layer bottom, vertically to the sea surface. This apportioning of the mixed layer is illustrated in Fig. 10 .

In MICOM, isopycnal mass fluxes are calculated in the course of solving the continuity equation. Diapycnal fluxes, defining the rate at which mass is exchanged between layers, represent the combined effect of mixed layer entrainment/detrainment, convective adjustment, and interior diapycnal mixing. (Note that bolus fluxes resulting from interface smoothing do not have a diapycnal component but rather are part of the isopycnal mass flux field.) All these mass flux contributions, together with changes in grid box height occurring where the 3D isopycnal/diapycnal mass flux field is not divergence-free, can be diagnosed and time-integrated in straightforward fashion in the course of a model run. The final outcome of this process is an internally consistent statement about the time-integrated mass flux across each of the six faces of every single grid box in (x, y, σ_2) space. This deluge of information needs to be reduced considerably before large-scale circulation patterns can be identified.

We have developed the following procedures for combining grid-scale mass fluxes into schematics of large-scale circulation patterns: Isopycnal mass fluxes across a line of grid points are "bundled" by first locating along the line in question the points where the normal mass flux changes sign, and then summing up the mass flux values over each interval so defined. We have found it convenient to display the bundled flux values in the form of variable-size arrows plotted at flux-weighted positions. The arrow size is intended to give a rough idea of the magnitude of the associated mass flux; the exact transport amount is written next to each arrow. This procedure is repeated for all north–south and east–west running grid lines.

Figure 11 gives examples of time averages of the zonal and meridional flux, respectively, obtained by the above procedure in the intermediate water class. To improve legibility, zonal/meridional flux arrows are only plotted for every second grid column/row. Note that the arrows constructed here do not represent vector components of a flux vector. In the case of a current running at a 45° angle across the grid, for example, both the zonal and the meridional flux arrow associated with this current will show its total strength, not the total strength divided by $(2)^{1/2}$ as would be the case if the arrows represented vector components in the true sense of the word.

Since diapycnal fluxes tend to be associated with isopycal mass flux divergences or convergences, the diapycnal flux fields often are less organized than the undifferentiated isopycnal fluxes themselves. We therefore subject the diapycnal flux fields to a "coagulation" process that replaces contoured diapycnal velocity fields (given in units of velocity, or Sv per unit area) with regionally integrated measures of vertical transport (in units of Sv). This coagulation process is analogous to the process of determining the volume of a mountain from the terrain height field on a topographic chart. Like in the case of the isopycnal fluxes, where cancellation of fluxes of different sign is avoided by summing up positive and negative contributions

separately, positive and negative "mountains" representing subduction/upwelling areas are area-integrated separately. Results of this procedure are not unique because they depend on a user-selectable length scale that specifies how close two "mountains" must be to be counted as one.

The algorithm that locates significant maxima and minima in a field of gridpoint values and combines these with surrounding grid values into regional integrals over the field in question works as follows.

1. A circular area centered on a given grid point (point A) is searched for the largest gridpoint value having the same sign as the value at A. If this maximum exceeds the value at A, point A is mapped onto the point where the maximum occurs (point B). The number of A points mapped onto each B point is recorded. A given B point can be an A point with respect to yet another B point.

2. All A points that do not belong to the set of B points are located. The value from each of these A points is added to the value at its associated B point. Thereafter, the A point in question is eliminated from the mapping registry. This elimination process includes subtracting 1 from the count of A points mapped onto the B point in question.

3. As A points are eliminated, some B points will lose their status as B points, but they may still be A points. Step 2 is repeated until no A points are left.

The remaining B points represent regional totals of the original gridpoint data. As indicated already, the resulting dataset is not unique because the area of integration depends to some extent on the search radius used in step 1. In the present work, a five-gridpoint search radius (7° in longitude) is used.

The final product of the above procedure is a set of values representing regional totals of diapycnal mass transport across a given interface. Figure 12 shows an example of this transport across the interface between the intermediate and deep water classes. Contour lines are the sea surface height (in units of cm). Transport values are given in units of 0.1 Sv; positive numbers indicate downward fluxes. In contrast to the vertical fluxes implied by the streamfunction plots in Fig. 5, the vertical flux fields shown in Fig. 12 represent genuine diapycnal motion.

Much diapycnal mass exchange occurs in the Southern Ocean, where deep layers outcrop into the mixed layer. This exchange does not take place directly between interior isopycnal layers but rather is mixed layer "mediated" in the sense that water parcels entering the mixed layer during winter are subjected there to density-changing processes and hence are not necessarily detrained in summer into the layer they came from.

Much of the diapycnal motion appears to be associated with stationary meanders of the ACC. A simple mechanistic explanation of this phenomenon is that meridionally moving water tends to be subjected to stronger thermal surface forcing than zonally moving water; thus, subduction and entrainment processes tend to be concentrated in locations where the prevailing flow has a meridional component. Given the approximations made in extending interior model layers across the mixed layer to the ocean surface (Fig. 10), the magnitude of the diapycnal transport associated with mixed layer subduction/entrainment cannot be easily quantified in our analysis.

Under nonsteady flow condition, local inconsistencies may arise between the horizontal and vertical flux display products because the fluxes through the six faces of a grid box in areas where layer thickening or thinning occurs will no longer add up to zero. Given the relative degree of steadiness in our model fields, this inconsistency is of no concern here.

g. The "plumbing" diagram

The flux plots described above yield information that has been reduced sufficiently to allow construction of a global ocean circulation diagram. If the zonal flux field in Fig. 11a is viewed in conjunction with the meridional flux field in Fig. 11b, a picture of current systems connecting all three major ocean basins emerges. These currents can be drawn as continuous threads and assigned specific transport amounts. Transport amounts, of course, are by no means constant along each thread. In fact, the most time-consuming task in constructing the circulation diagram is to distinguish current strength variations caused by horizontal recirculation loops from variations attributable to diapycnal mass transport. This typically turns into an iterative process that defies attempts at automation.

We have found it advantageous to begin the process by labeling each horizontal circulation segment with the maximum transport value diagnosed along it. In other words, we try to draw a circulation diagram that accommodates the *peak* values. We then try to explain as many of the longstream transport variations as possible by the presence of recirculation loops. Finally, we overlay the horizontal flux map with the condensed diapycnal flux fields to determine whether horizontal flux imbalances can be explained in terms of mass exchange with classes above or below. Since the horizontal threads represent abstractions of a continuous two-dimensional flow field, transport imbalances along the threads are not always collocated with regions of diapycnal flux. This complicates matters further.

In our experience, the task of associating horizontal current strength fluctuations with diapycnal fluxes becomes easier if the flux information contained in Figs. 11 and 12 ⊙ is supplemented by more coarse-grained information, such as the total flux across latitude circles and parallels between pairs of coastal points, and diapycnal fluxes integrated coast-to-coast over single grid rows or columns. The spatial consistency found in these additional fields also reassures the analyst that the model as a whole conserves mass.

We refer to the synthesized mass transport diagrams that are the outcome of this effort as *plumbing* diagrams. They are shown in Fig. 13 ⊙ for the upper, intermediate, deep, and bottom class in the colors purple, red, green, and blue, respectively, following the color scheme of Schmitz (1995). The numbers in circles and pentagons are transport amounts in Sverdrups. Circled numbers represent horizontal transport within a class, while numbers enclosed in upward- and downward-pointing pentagons represent diapycnal transport between classes in the direction indicated.

h. Modeled mass fluxes and their comparison to observations

Meridional mass transports in/across each class in each basin, based on the model output as illustrated in Figs. 11 and 12 ⊙ are presented in Figs. 14, 15, and 16 ⊙ for the Atlantic, Pacific, and Indian Ocean, respectively. Tables 1, 2, and 3 ⊙ show the meridional mass transport at 32°S in the Atlantic, Pacific, and Indian basins from the model output and comparisons with observations.

1) ATLANTIC OCEAN

The westward-intensified wind-driven subtropical gyre circulation, the Gulf Stream system, is a prominent feature in both the upper and intermediate class with a combined transport of 72 Sv. There are 14 Sv and 4 Sv of northward flow across the equator in the upper and intermediate class, respectively, which compensate the 8 Sv and 10 Sv southward flow in the deep and bottom class. The diapycnal mass exchange in the Atlantic is dominated by upwelling near the equator and downwelling at high latitudes.

Strong downwelling occurs in the Labrador Sea, with 6 Sv descending from the intermediate to the deep class and 4 Sv from the deep to the bottom class. The latter figure is supplemented by the 6 Sv of downward flux imposed along the boundary between Greenland and Norway.

The strong downwelling in the northern North Atlantic is the main source of southward flowing NADW, roughly as suggested by Schmitz and McCartney (1993) and the classical studies mentioned in the introduction. The 18-Sv southward flow in the deep and bottom classes combined is at the low end of estimates of deep western boundary current transport based on observed data, namely 25 Sv at 10°N (Speer and McCartney 1991), 26 Sv below the 4.7°C surface for the most intense portion of the DWBC (Molinari et al. 1992), and 18 Sv crossing the equator (Schmitz 1995). In the North Atlantic, Lower NADW transport, seen in the bottom class, dominates over Middle NADW transport, seen in the deep class, while the opposite is true in the South Atlantic, owing to the fact that 3 Sv are converted from Lower to Middle NADW near the equator. This is consistent with the hemispheric asymmetry seen in observations by Friedrichs et al. (1994).

Two prominent features in the bottom density class, which are inconsistent with observations, are the apparent formation of bottom water in the Labrador Sea and insufficient northward penetration of bottom water generated in the Southern Ocean. The first problem may in part be caused by the exclusion of overflow entrainment of deep ambient subpolar gyre water. The failure of AABW to move northward past the Argentine Basin may arise because AABW formation, which is specified as a lateral boundary condition, is inconsistent with the large-scale circulation. The tendency of primitive equation models to "marginalize" the effect of imposed lateral boundary conditions is well known (Klinck 1995).

Table 1 ⊙ shows that the meridional mass transport at 32°S in the model Atlantic agrees well with Rintoul's (1991) estimates in Table 1 ⊙ except for the sign reversal in the bottom layer, which is due to the absence of northward flowing AABW.

2) PACIFIC OCEAN

The strong boundary current associated with the subtropical gyre in the North Pacific, the Kuroshio, carries a total 58 Sv of upper and intermediate water combined. Near the equator, the Equatorial Undercurrent dominates with 31 Sv transport, which is probably too high due to coarse horizontal resolution. Four Sv of bottom water flowing alongside the Tonga Escarpment into the Pacific are converted to deep water in the southern and northern Pacific. A total of 6 Sv of deep water enter the Pacific from the ACC. Combined with 4 Sv gained from the bottom layer, there are 2 Sv and 3 Sv of deep water that upwell near the equator and in the North Pacific, respectively. The remaining 5 Sv return as a poleward flow along the eastern boundary of the Pacific and join the ACC west of Drake Passage, as noted by Reid (1986). The intermediate water class gains a total of 5 Sv through upwelling from below and 1 Sv from above. All of that water flows into the Indian

Ocean—3 Sv through the Indonesian Passage and the rest clockwise around Australia.

In comparison to a 6-layer classification used by Toole et al. (1994b) (reproduced here as Table 4 ⊙▪), our model results in the South Pacific shown in Table 2 ⊙▪ indicate too strong a northward branch and too weak a southward branch in the deep water, the latter corresponding to the dominant eastern boundary current noted in Toole et al. (1994b). In contrast, the bottom water inflow is much smaller than observed (Toole et al. 1994b).

3) INDIAN OCEAN

In the upper two classes, the southward flow through the Mozambique Channel is 29 Sv, and the Agulhas Current has a transport of about 99 Sv. The Agulhas separates into two branches near the Cape of Good Hope, one flowing into the South Atlantic with a strength of 37 Sv (21 Sv and 16 Sv in the upper and intermediate class, respectively), the remaining 62 Sv (24 Sv and 38 Sv, respectively) turning east and joining the ACC in the so-called Agulhas Retroflection.

In the deep class, 7 Sv of ACC water branch off and turn northward into the Indian Ocean. Of these, 4 Sv follow an eastern path and 3 Sv a western path, as illustrated in the tracer plots in Figs. 9c and 9d ⊙▪. An additional 2 Sv of ACC water in the bottom class enter the Indian Ocean along the Ninety East Ridge. The model flow pattern agrees reasonably well with observations (Mantyla and Reid 1995; Schmitz 1996b; Robbins and Toole 1997). Seven out of 9 Sv of deep and bottom water combined upwell near the equator in the Indian Ocean.

Although the model is able to describe some realistic circulation features, and the flows in the upper two classes as well as the total net flow across 32°S in the Indian Ocean are close to the estimate of Robbins and Toole (1997) (see Table 3 ⊙▪), the distribution of the flow among the lower two categories reveals discrepancies. The model develops an inflow in both the deep and bottom class, 5 Sv and 2 Sv, respectively. Compared to Robbins and Toole (1997), both the northward bottom flow and the southward deep flow are too weak.

4) INTERBASIN AND SOUTHERN OCEAN

Table 5 ⊙▪ shows the interbasin mass exchanges estimated by various authors. According to studies by Fieux et al. (1996) based on geostrophic transport arguments, the Indonesian Throughflow is 18 ± 7 Sv in August 1989 and −2.6 ± 9 Sv in February 1992. These values match those of the Meyers (1996) expendable bathythermograph measurements, which show the two extremes of opposite sign in a 10-yr low-frequency variation study covering the El Niño year 1992 and the non-El Niño year 1989. The annual mean Indonesian Throughflow transport of 12 Sv obtained from the model forced by climatology agrees well with these indirect observations, but is higher than the 8 Sv from Schmitz (1996a).

Observations of the Agulhas Current transport also show a wide range, caused in part by variations in the geographic location of the observing site. Observation by Jacobs and Georgi (1977) and Bennett (1988), which were taken near the latitude where the model gives a 99 Sv transport, range from 97 to 137 Sv, and an estimate from Macdonald (1998) gives 93 ± 2 Sv. Sixty-two Sverdrups of the total Agulhas transport return to the Indian Ocean in the model, smaller than the 85 Sv retroflection value observed by Gordon et al. (1987). The weak retroflection near the Cape of Good Hope allows 37 Sv of Agulhas water to join the subtropical gyre circulation in the South Atlantic. This value is probably excessive.

The 108 Sv throughflow in the Drake Passage obtained in the model, with a distribution of 8 Sv, 41 Sv, 57 Sv, and 2 Sv in the upper, intermediate, deep, and bottom class, respectively, is slightly lower than the 123 ± 10.5 Sv observed by Whitworth and Peterson (1985).

5) INTERBASIN EXCHANGE DIAGRAM

Since the horizontal gyre circulation engaged in heat exchange with the atmosphere has a "vertical" (namely, diapycnal) component if viewed in density space, the thermohaline-forced circulation cannot totally be decoupled from the wind-forced circulation, both in the real world and in isopycnic coordinate models. In order to obtain an approximate map of the thermohaline component, the horizontal recirculation loops in each basin in the upper two classes have been removed, under the assumption that these represent the wind-driven portion of the circulation. The resulting diagram of what may be called interbasin water mass exchange is shown in Fig. 17 ⊙▪.

In comparing this map to the thermohaline circulation chart of Schmitz (1995), many similarities are seen, even though inconsistencies between Schmitz's and our four water classes give rise to unavoidable differences. In the Atlantic, the formation rate of the NADW and its compensatory flow in the upper two classes are similar, although the northward flowing AABW is missing in the model. A total of 10 Sv of bottom water reach the equatorial Pacific in Schmitz (1995), while in the model the 10-Sv inflow is distributed over the deep and bottom water classes. The Indonesian Throughflow rate in the upper class is similar, but the model shows an additional 3 Sv in the intermediate class. More discrepancies are found

in the Indian Ocean where the model generates 7 Sv of inflow of deep and bottom water combined, while Schmitz (1995) shows a 24 Sv inflow of bottom water, more than what is shown in Robbins and Toole (1997) (see Table 4). The Agulhas Current in the model is much stronger than in Schmitz (1995) (42 Sv vs 22 Sv), mainly because the Agulhas branch directed by the model into the Atlantic—where it eventually "retroflects" at the South American coast—does not qualify as an intrabasin gyre and thus could not be subtracted from the Agulhas total shown in Fig. 13 . Overall, most of the discrepancies are AABW related. A comparison of the water mass transport in four classes in several regions is given in Table 6 .

4. Discussion

This paper presents a first effort at quantifying the thermohaline-forced circulation in a millennial, near-global, coarse-mesh simulation performed with an isopycnic coordinate model forced by monthly varying atmospheric state variables. (Emphasis here is on the word *atmospheric.* Relaxation toward an observed *oceanic* state, a commonly used device to suppress model drift in long-term simulations, was not employed.)

Regional features of the three-dimensional ocean circulation, to the extent that they can be resolved in a coarse resolution model, have been condensed into "plumbing diagrams" that attempt to imitate the display style employed by Schmitz (1995, 1996a,b). The first diagram, Fig. 13 , exhibits all of the well-known western boundary currents and wind-driven gyres. The transport amounts associated with these gyres tend to be slightly low, reflecting linear Sverdrup dynamics, since the model's 1.4° mesh does not adequately resolve small recirculation gyres. The second diagram, Fig. 17 , was derived from the first one by omitting circulation cells confined to single ocean basins.

The global interbasin water mass exchange (Fig. 17) is of roughly the observed amplitude and occurs approximately along the paths suggested by various observational summaries (e.g., Gordon 1986; Mantyla and Reid 1995; Rintoul 1991; Robbins and Toole 1997; Schmitz 1995, 1996a,b). At the next level of detail, the transport of NADW (18 Sv) approaching the equator is close to observation, but the mechanism of NADW formation in the model may be deficient; in particular, AABW does not penetrate northward in the model to contribute to the properties of lower NADW. The model approximation to Lower NADW upwells to "Middle NADW" in the equatorial Atlantic, a feature at least to some extent consistent with the analysis of Friedrichs et al. (1994).

Meridional sections of the thermohaline circulation in each ocean basin are given in Figs. 14–16 . They show the water mass balance between the upwelling/downwelling and the horizontal transports in each of the four classes. As shown in Fig. 17 , two main "upper branch" pathways support NADW formation: 14 Sv and 4 Sv from the upper and intermediate class, respectively. Among the 14 Sv, at least 5 Sv come from the Indian Ocean, together with the 8 Sv from Drake Passage and 1 Sv upwelling from below. The source of the 4 Sv intermediate water cannot be determined from our analysis due to the homogenizing action of the South Atlantic subtropical gyre. We can state, however, that the current feeding the NADW production mechanism represents a combination of both warm and cold path inflows.

Two noteworthy model results that to some extent are in accord with the database are the equatorial conversion of Lower NADW to a less dense deep water in the Atlantic (see Friedrichs et al. 1994) and the transformation of bottom water from the ACC entering both the South Pacific and the South Indian to deep water in the equatorial Pacific, and Indian Ocean, respectively. Another model result worth noting is the flow of 7 Sv of deep water into the South Indian Ocean from the Circumpolar Current in the vicinity of Australia, with 3 Sv flowing northward east of Madagascar. The remaining 4 Sv of deep water flowing north along the Ninety East Ridge (Mantyla and Reid 1995; Robbins and Toole 1997) is converted to intermediate water in the tropical Indian Ocean, eventually reaching the Atlantic through the Agulhas Current.

Among the discrepancies between model results and current observational estimates of the global THC, the most prominent one concerns the amount of bottom water spreading northward from the Southern Ocean. Toole et al. (1994b), for example, find 13 Sv of bottom water flowing north as a western boundary current in the Pacific Ocean across 32°S, 12 Sv of which recirculate southward across 32°S as deep water, presumably to rejoin the ACC. This vertical–meridional circulation is much stronger in the observations than in the model (Fig. 17). In fact, as can be seen from Tables 1, 2, and 3 , the northward bottom water flow is weaker than observed in all three basins. As a result of this, the southward flow in the deep class is weaker as well.

The most likely cause of the aforementioned deficiency is the model's inability to produce bottom water around Antarctica at a high enough rate. Figure 13 indicates that southern bottom-water formation would, in fact, be zero were it not for the 3 Sv of imposed diapycnal flux in the Weddell Sea. In other words, nowhere along the Antarctic continent are the freshwater and thermal boundary conditions used in this particular simulation capable of producing water dense enough to fit into our bottom water category.

Observational estimates of the AABW formation rate vary widely. Orsi et al. (1999) deduce a rate of 8–9 Sv from Chlorofluorocarbon measurements. Peacock et al. (2000) find that a production rate of 15 ± 4 Sv is needed to reconcile

measurements of four different abyssal tracers. Ganachaud and Wunsch (2000) deduce from their inverse model a production rate of 21 ± 6 Sv for Circumpolar Deep Water, a water mass category somewhat broader than AABW but resembling our bottom water class.

In our experience and that of other modeling groups, maintaining a CDW production rate of 10–20 Sv requires utmost care (and, given the observational uncertainties, a good portion of luck) in striking the correct balance between external forces, such as glacier runoff and heat loss to the atmosphere, and model-intrinsic processes such as ice formation and meridional salt and heat transport across the ACC. The last-mentioned factor is particularly troublesome as it makes this balance sensitive to horizontal (eddy vs noneddy resolving) grid resolution. Given the paucity of observations addressing details of the atmospheric forcing around Antarctica, especially during winter, and the lack of a sea ice module in the MICOM version used here, it is perhaps not surprising that the present simulation misses the mark on CDW production.

Various studies (e.g., Toole et al. 1994a) have pointed out that rough topography can dramatically enhance diapycnal mixing in the deep ocean. The diapycnal mixing coefficient used in this model run, 0.002 $(cm^2 \, s^{-2})/N$, is not a function of bottom roughness. This may weaken the upwelling in the seamount-filled Indian Ocean. As a result, some water that in reality flows into and upwells in the Indian Ocean may upwell in the ACC or the Pacific.

Efforts to refine today's cursory parameterization of diapycnal diffusion by taking into account factors such as tidal amplitude and bottom roughness are still in their infancy. Until these techniques mature, the goal of correctly modeling the formation rate of individual water masses will remain elusive.

Our results point at shortcomings in the present simulation that need to be addressed in future experiments. The leading candidates on this list are omission of the Arctic Ocean, lack of a sea ice component, insufficient knowledge of diapycnal mixing, and the poor quality of surface boundary conditions.

One of the major challenges we have met in the course of this study, as one would in any modeling effort, is dealing with the incomplete and perhaps inaccurate observational datasets. First, there are problems with spatial data coverage due to the wide separation of ship routes in some ocean basins. Many gaps in the data coverage had to be filled artificially. This is especially the case in the Southern Ocean. Secondly, sea surface conditions are infrequently sampled. The climatological monthly mean estimates derived from such data preclude synoptic-scale atmospheric phenomena, such as arctic lows, which may regionally and temporarily enhance deep-water formation. During the passage of frontal systems, sea surface cooling leads to deeper mixing that preconditions the water column for subsequent downwelling. The absence of such "weather" in the forcing data probably weakens deep-water formation rates in the model. This is one likely reason—aside from the truncated domain and the poor observed data coverage in the Southern Ocean—why the present MICOM implementation does not produce enough bottom water.

One remedy for inaccurately known atmospheric forcing functions would be to couple the ocean model to an atmospheric model, but this would allow atmospheric model errors and biases, of which there are many, to affect the oceanic circulation.

REFERENCES

Bennett S. L., 1988: Where three oceans meet: The Agulhas retroflection region. Ph.D. dissertation, Woods Hole Oceanographic Institution and Massachusetts Institute of Technology, 367 pp.

Bleck R., 1998: Ocean modeling in isopycnic coordinates. *Ocean Modeling and Parameterization,* E. P. Chassignet and J. Verron, Eds., NATO Science Series C, Vol. 516, Kluwer, 423–448.

Bleck R., C. Rooth, D. Hu, and L. Smith, 1992: Salinity-driven thermocline transients in a wind- and thermohaline-forced isopycnic coordinate model of the North Atlantic. *J. Phys. Oceanogr*, **22**, 1486–1505. Find this article online

Bleck R., S. Sun, and S. Dean, 1997: Global ocean simulations with an isopycnic coordinate model. *Some New Directions in Science on Computers,* G. Bhanot, S. Chen, and P. Seiden, Eds., World Scientific, 297–317.

Broecker W. S., 1991: The great ocean conveyor. *Oceanography*, **4**, 79–89. Find this article online

Brown J., A. Colling, D. Park, J. Phillips, D. Rothery, and J. Wright, 1989: Global fluxes and deep circulation. *Ocean Circulation,* G. Bearman, Ed., Pergamon, 159–208.

Chassignet E. P., L. T. Smith, R. Bleck, and F. O. Bryan, 1996: A model comparison: Numerical simulations of the north and equatorial Atlantic oceanic circulation in depth and isopycnic coordinates. *J. Phys. Oceanogr*, **26**, 1849–1867. Find this article online

Döös K., 1995: Interocean exchange of water masses. *J. Geophys. Res*, **100**, 13499–13514. Find this article online

Fieux M., R. Molcard, and A. G. Ilahude, 1996: Geostrophic transport of the Pacific–Indian Oceans throughflow. *J. Geophys. Res*, **101**, 12421–12432. Find this article online

Friedrichs M. A. M., M. S. McCartney, and M. M. Hall, 1994: Hemispheric asymmetry of deep water transport modes in the Atlantic. *J. Geophys. Res*, **99**, 25165–25179. Find this article online

Ganachaud A., and C. Wunsch, 2000: Improved estimates of global ocean circulation, heat transport and mixing from hydrographic data. *Nature*, **408**, 453–457. Find this article online

Gent P. R., and J. C. McWilliams, 1990: Isopycnal mixing in ocean circulation models. *J. Phys. Oceanogr*, **20**, 150–155. Find this article online

Gordon A. L., 1986: Interocean exchange of thermocline water. *J. Geophys. Res*, **91**, 5037–5046. Find this article online

Gordon A. L., J. R. E. Lutjeharms, and M. L. Gründlingh, 1987: Stratification and circulation at the Agulhas Retroflection. *Deep-Sea Res*, **34**, 565–599. Find this article online

Jacobs S. S., and D. T. Georgi, 1977: Observations on the Southwest Indian/Antarctic Ocean. *A Voyage of Discovery,* George Deacon 70th Anniversary Volume, M. Angel, Ed., *Deep-Sea Res*, **24**, 43–84, (Suppl.). Find this article online

Klinck J. M., 1995: Thermohaline structure of an eddy-resolving North Atlantic model. The influence of boundary conditions. *J. Phys. Oceanogr*, **25**, 1174–1195. Find this article online

Levitus S., and T. P. Boyer, 1994: *World Ocean Atlas 1994*. Vol. 4: *Temperature,* NOAA, 117 pp.

Levitus S., R. Burgett, and T. P. Boyer, 1994: *World Ocean Atlas 1994*. Vol. 3: *Salinity,* NOAA, 99 pp.

Macdonald A. M., 1998: The global ocean circulation: A hydrographic estimate and regional analysis. *Progress in Oceanography,* Vol. 41, Pergamon, 281–382.

Macdonald A. M., and C. Wunsch, 1996: An estimate of global ocean circulation and heat fluxes. *Nature*, **382**, 436–439. Find this article online

Mantyla A. W., and J. L. Reid, 1995: Origins of deep and bottom waters of the Indian Ocean. *J. Geophys. Res*, **100**, 2417–2439. Find this article online

Mauritzen C., 1993: A study of the large scale circulation and water mass formation in the Nordic Seas and Arctic Ocean. Ph.D. dissertation, Massachusetts Institute of Technology and Woods Hole Oceanographic Institution, 212 pp.

Mauritzen C., 1996a: Production of dense overflow waters feeding the North Atlantic across the Greenland–Scotland Ridge. Part 1: Evidence for a revised circulation scheme. *Deep-Sea Res*, **43**, 769–806. Find this article online

Mauritzen C., 1996b: Production of dense overflow waters feeding the North Atlantic across the Greenland–Scotland Ridge. Part 2: An inverse model. *Deep-Sea Res*, **43**, 807–835. Find this article online

McDougall T. J., and W. K. Dewar, 1998: Vertical mixing and cabbeling in layered models. *J. Phys. Oceanogr*, **28**, 1458–1480. Find this article online

Meyers G., 1996: Variations of Indonesian Throughflow and the El Niño–Southern Oscillation. *J. Geophys. Res*, **101**, 12255–12263. Find this article online

Molinari R. L., R. A. Fine, and E. Johns, 1992: The deep western boundary current in the tropical North Atlantic Ocean. *Deep-Sea Res*, **39**, 1967–1984. Find this article online

Oberhuber J. M., 1988: An atlas based on the "COADS" data set: The budgets of heat, buoyancy, and turbulent kinetic energy at the surface of the global ocean. Max-Planck-Institut für Meteorologie, Hamburg, Germany, 202 pp.

Orsi A. H., G. C. Johnson, and J. L. Bullister, 1999: Circulation, mixing, and production of Antarctic Bottom Water. *Progress in Oceanography,* Vol. 43, Pergamon, 55–109.

Peacock S., M. Visbeck, and W. Broecker, 2000: Deep water formation rates inferred from global tracer distributions: An inverse approach. *Inverse Methods in Global Biogeochemical Cycles, Geophys. Monogr.*, No. 114, Amer. Geophys. Union, 185–195.

Price J. F., and M. O'N. Baringer, 1994: Outflows and deep water production by marginal seas. *Progress in Oceanography,* Vol. 33, Pergamon, 161–200.

Reid J. L., 1986: On the total geostrophic circulation of the South Pacific Ocean: Flow patterns, tracers and transports. *Progress in Oceanography,* Vol. 16, Pergamon, 1–61.

Rintoul S. R., 1991: South Atlantic interbasin exchange. *J. Geophys. Res*, **96**, 2675–2692. Find this article online

Robbins P. E., and J. M. Toole, 1997: The dissolved silica budget as a constraint on the meridional overturning circulation of the Indian Ocean. *Deep-Sea Res*, **44**, 879–906. Find this article online

Roberts M. J., R. Marsh, A. L. New, and R. A. Wood, 1996: An intercomparison of a Bryan–Cox-type ocean model and an isopycnic ocean model. Part I: The subpolar gyre and high-latitude processes. *J. Phys. Oceanogr*, **26**, 1495–1527. Find this article online

Schmitz W. J. Jr., 1995: On the interbasin-scale thermohaline circulation. *Rev. Geophys*, **33**, 151–173. Find this article online

Schmitz W. J. Jr., 1996a: On the World Ocean circulation. Vol. I: Some global features/North Atlantic Circulation. Woods Hole Oceanographic Institution Tech. Rep. WHOL-96-03, 140 pp.

Schmitz W. J. Jr., 1996b: On the World Ocean circulation. Vol. II: The Pacific and Indian Oceans/A global update. Woods Hole Oceanographic Institution Tech. Rep. WHOI-96-08, 237 pp.

Schmitz W. J. Jr., and M. S. McCartney, 1993: On the North Atlantic circulation. *Rev. Geophys*, **31**, 29–49. Find this article online

Smethie W. S., R. A. Fine, A. Putzka, and P. Jones, 1999: Tracing the flow of North Atlantic Deep Water using chlorofluorocarbons. *J. Geophys. Res*, **105**, 14297–14323. Find this article online

Speer K. G., and M. S. McCartney, 1991: Tracing lower North Atlantic Deep Water across the equator. *J. Geophys. Res*, **96,**, 20443–20448. Find this article online

Speer K. G., and W. Zenk, 1993: The flow of Antarctic bottom water into the Brazil Basin. *J. Phys. Oceanogr*, **23**, 2667–2682. Find this article online

Spencer R. W., 1993: Global oceanic precipitation from the MSU during 1979–91 and comparisons to other climatologies. *J. Climate*, **6**, 1301–1326. Find this article online

Stommel H., 1957: A survey of ocean current theory. *Deep-Sea Res*, **4**, 149–184. Find this article online

Stommel H., 1964: The large-scale oceanic circulation. *Advances in Earth Science,* P. M. Hurley, Ed., The MIT Press, 175–184.

Stommel H., 1965: *The Gulf Stream, A Physical and Dynamical Description*. 2d ed. University of California Press, 248 pp.

Sun S., 1997: Compressibility effects in the Miami Isopycnic Coordinate Ocean Model. Ph.D. dissertation, University of Miami, 138 pp.

Sun S., R. Bleck, C. G. H. Rooth, J. Dukowicz, E. P. Chassignet, and P. Killworth, 1999: Inclusion of thermobaricity in isopycnic-coordinate ocean models. *J. Phys. Oceanogr*, **29**, 2719–2729. Find this article online

Toole J. M., K. L. Polzin, and R. W. Schmitt, 1994a: Estimates of diapycnal mixing in the abyssal ocean. *Science*, **264**, 1120–1123. Find this article online

Toole J. M., S. E. Wijffels, M. S. McCartney, B. A. Warren, H. L. Bryden, and J. A. Church, 1994b: WOCE hydrographic section P6 across the subtropical South Pacific Ocean. *Proc. Pacific Basin Meeting,* Honolulu, HI, The Oceanography Society, 76.

Trenberth K. E., and A. Solomon, 1994: The global heat balance: Heat transports in the atmosphere and ocean. *Climate Dyn*, **10**, 107–134. Find this article online

Whitworth T. III, and R. G. Peterson, 1985: Volume transport of the Atlantic Circumpolar Current from bottom pressure measurements. *J. Phys. Oceanogr*, **15**, 810–816. Find this article online

Woodruff S. D., R. J. Slutz, R. L. Jenne, and P. M. Steurer, 1987: A comprehensive ocean–atmosphere data set. *Bull. Amer. Meteor. Soc*, **68**, 1239–1250. Find this article online

Tables

TABLE 1. Northward mass transport (Sv) across 32°S in the Atlantic estimated by the model and Rintoul (1991)

Class	Model	Rintoul (1991)
Upper	14	8
Intermediate	4	5
Deep	−8	−17
Bottom	−10	4

Click on thumbnail for full-sized image.

TABLE 2. Northward mass transport (Sv) across 32°S in the Pacific estimated by the model and Toole et al. (1994b)

Class	Model	Toole et al. (1994b)
Upper	10	10
Intermediate	−3	0
Deep	1	−12
Bottom	4	13
Net	12	11

Click on thumbnail for full-sized image.

TABLE 3. Northward mass transport (Sv) across 32°S in the Indian estimated by the model and Robbins and Toole (1997)

Class	Model	Robbins and Toole (1997)
Upper	−10	−12
Intermediate	−9	−7
Deep	5	−2
Bottom	2	11
Net	−12	−10

Click on thumbnail for full-sized image.

TABLE 4. Northward mass transport (Sv) across 32°S in the Pacific. Reproduced from Toole et al. (1994b)

Layer	Water types	Net transport (Sv)
1	Thermocline waters	9.9
2	Antarctic Intermediate Water	6.7
3	Equatorial water (east), AAIW (west)	−7.0
4	North Pacific Deep Water and lower circumpolar water	−12.0
5	Returning lower circumpolar water	−3.7
6	Densest of the lower circumpolar water (AABW)	16.5
Total		10.5

Click on thumbnail for full-sized image.

TABLE 5. Interbasin mass exchanges (Sv) estimated by different studies

	Indonesian passage	Agulhas	Agulhas retroflection	Drake Passage
Fieux et al. (1996)	−2.6 ± 9 to 18 ± 7			
Macdonald (1998)		93 ± 2		
Gordon et al. (1987)			85	
Whitworth et al. (1982)				130
MICOM (1.4°)	12	99	62	108

Click on thumbnail for full-sized image.

TABLE 6. Northward mass transport (Sv) in four classes, estimated by Schmitz (1995) and from the present experiment. Thermohaline component only

	Equatorial Atlantic	Indonesian passage	Agulhas Current
Schmitz (1995)	9, 5, −18, 4	8, 0, 0, 0	8, 10, 4, 0
MICOM (1.4°)	14, 4, −8, 10	9, 3, 0, 0	21, 19, 2, 0

Click on thumbnail for full-sized image.

Figures
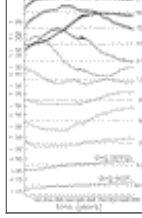
FIG. 1. Deviation of individual horizontally averaged layer thickness (upper 16 curves) from its horizontal temporal mean and globally averaged temperature/salinity (bottom two curves) from global temporal mean, plotted against time. Some ordinate labels omitted to avoid crowding. Numbers on the right indicate horizontal or global temporal mean
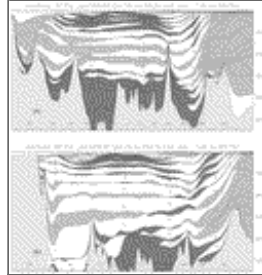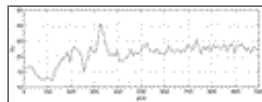
FIG. 2. Layer interfaces from run A in model year 1 (dashed) and model year 1000 (solid) along meridional sections in the Atlantic (a) and Pacific (b). Light/dark shading indicates interface descent/rise during time interval. Layer indices are centered on layers at final time
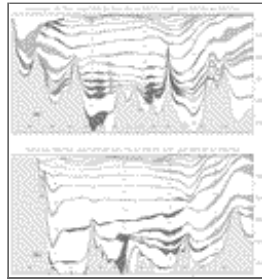
FIG. 3. As in Fig. 2 ⬤= but for years 900–1000

FIG. 4. Census of maximum overturning rate in Atlantic in the experiment
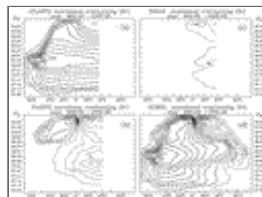
FIG. 5. Zonally integrated, 100-yr averaged meridional overturning streamfunction (Sv): (a) Atlantic Ocean, (b) Pacific Ocean, (c) Indian Ocean, and (d) global ocean
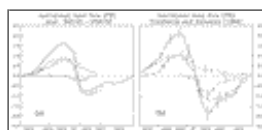
FIG. 6. Zonally integrated meridional heat flux in PW (1 PW = 10^{15} W) plotted against latitude (a) from the model and (b) From Trenberth and Solomon (1994): GL, PA, AT, and IN refer to Global, Pacific, Atlantic, and Indian Ocean, respectively
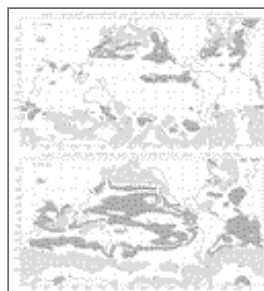
Click on thumbnail for full-sized image.

FIG. 7. Surface drift during the 1000-yr run: (a) sea surface-temperature and (b) sea surface salinity
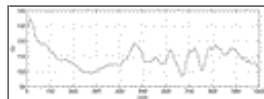
Click on thumbnail for full-sized image.

FIG. 8. Census of annual Drake Passage throughflow in the 1000-yr run
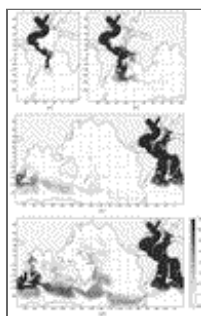
Click on thumbnail for full-sized image.

FIG. 9. Tracer (equivalent depth, m) continually injected into layer $\sigma_2 = 37.01$ at outcropping locations in the Labrador Sea: Year 25 (a), year 50 (b), year 100 (c), and year 200 (d). Note logarithmic grayscale
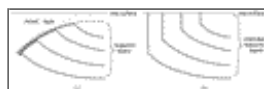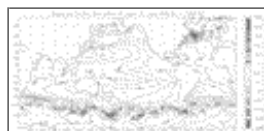

Click on thumbnail for full-sized image.

FIG. 10. Sketch of model layer structure (a) as used in the model integration and (b) as used for present mass flux diagnostics
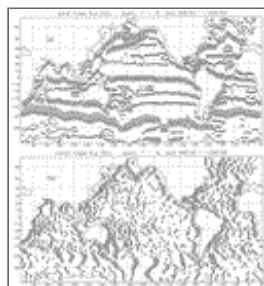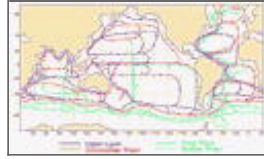

Click on thumbnail for full-sized image.

FIG. 11. Regionally integrated, 100-yr averaged zonal mass flux (Sv) in the intermediate class (36.37 $\leq \sigma_2 \leq$ 36.79): (a) zonal component and (b) meridional component
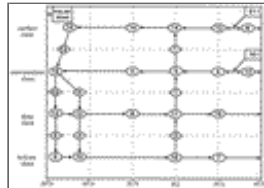

Click on thumbnail for full-sized image.

FIG. 12. Numbers represent regionally integrated, 100-yr averaged diapycnal mass flux (0.1 Sv) through interface between layers in the upper and intermediate classes. Positive numbers indicate downwelling. Contour lines show the sea surface height (cm). Shading represents velocity (m yr^{-1}) through the same interface
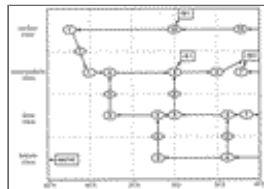

Click on thumbnail for full-sized image.

FIG. 13. Schematic of 100-yr averaged global ocean circulation (Sv) for years 900–1000 spanning the four density classes. Circled numbers represent transport within a class; numbers in pentagons represent transport across class boundaries
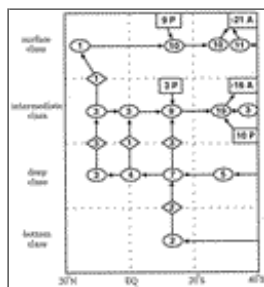

Click on thumbnail for full-sized image.

FIG. 14. Meridional mass transport (Sv) in four classes in the Atlantic basin, based on Fig. 13 ⊙. Circled numbers represent transport within classes, numbers in diamonds and squares represent transport between classes and across basin boundaries, respectively. Letter "I" indicates mass exchanges with the Indian Ocean
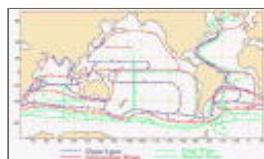

Click on thumbnail for full-sized image.

FIG. 15. As in Fig. 14 ⊙ but for the Pacific basin

Click on thumbnail for full-sized image.

FIG. 16. As in Fig. 14 ⊙ but for the Indian basin. Letter "A" and "P" indicate mass exchanges with the Atlantic and Pacific Ocean, respectively

Click on thumbnail for full-sized image.

FIG. 17. The interbasin exchange part of the circulation shown in Fig. 13 ⊙

Corresponding author address: Dr. Shan Sun, NASA Goddard Institute for Space Studies, 2880 Broadway, New York, NY 10025. E-mail: ssun@giss.nasa.gov

[1] The terms "bottom," "deep," and "intermediate," as used in this paper, will be defined in .